Illuminating the Motions of Jupiter's Auroral Dawn Storms

M. J. Rutala[1], J. T. Clarke[1,2], J. D. Mullins[1], J. D. Nichols[3]

[1]Department of Astronomy, Boston University, Boston, USA
[2]Center for Space Physics, Boston University, Boston, USA
[3]Department of Physics and Astronomy, University of Leicester, Leicester, UK

Key Points:

- A novel, fully automated method to identify and measure discrete auroral features in Jupiter's auroral main emission is described.
- Nearly five times more auroral forms are found to significantly lag behind rigid corotation in the dawn sector than expected.
- Jovian auroral theories must be expanded to better explain the enigmatic motions of dawn auroral features, which are too common to ignore.

Corresponding author: M. J. Rutala, `mrutala@bu.edu`

Abstract

Jupiter's auroral main emission (ME) has long been considered to be the result of currents keeping plasma corotating with the surrounding magnetosphere. As a result, the ME corotates with the planet, and individual auroral features making up the ME roughly follow suit. Jupiter's dawn storms, some of the rarest and brightest auroral features within the ME, are an exception, as they do not corotate but instead remain fixed near local dawn. The causes of this enigmatic motion are not fully understood. To test the significance of this motion, we have developed a process to identify auroral features and measure their degree of corotational motion, including dawn storms, in archival Hubble Space Telescope images of the Jovian ultraviolet aurorae. We compare motions of features inside and outside the dawn sector, characterizing the exact motions of dawn storms and providing context for these motions for the first time. In keeping with previous studies, we expected to identify features fixed near local dawn in 10% of observations; instead, we find that half of all features near local dawn lag corotation. We show that subcorotating dawn emissions are far more common than previously thought, and that the drivers of this motion must be similarly common. Corotational motion must be considered when identifying the processes driving all dawn aurorae, including the dawn storms. We explore the consistency of this result with various theories of dawn ME formation and propose that aspects of the known current system relating to the Sun-Jupiter geometry can explain this behavior.

Plain Language Summary

Jupiter's aurorae vary widely in brightness, shape, and motion across the planet. The brightest part of these aurorae, the main emission, consists of two ovals of nearly permanent lights partially surrounding the northern and southern magnetic poles, superficially similar to the auroral ovals of the Earth. This portion of the aurorae is thought to be created by the interaction of Jupiter's powerful magnetic field, fast rotation rate, and plasma produced from material ejected by the volcanic moon Io. This system as a whole moves at about the same speed as Jupiter's rotation, so it is expected that the aurorae would also rotate at this speed, appearing fixed in Jupiter's atmosphere. Dawn storms– rare, bright aurorae that appear near local dawn– seem to conflict with this picture. These storms move slower than the planet rotates, appearing to remain fixed near dawn. Here, we measure the rotation rates of auroral features across Jupiter to understand how often dawn storms occur and how significant their motion is. We find that auroral features often move slower than Jupiter's rotation rate throughout the dawn sector, which is surprising considering the rarity of dawn storms and that most auroral features are expected to match Jupiter's rotation.

1 Introduction

Jupiter's ultraviolet (UV) aurorae comprise essentially three large-scale components; in order of increasing latitude, these are: the satellite footprints, the main emission (ME), and the polar emissions (Clarke et al., 2004; Nichols et al., 2009; Grodent, 2015). Occasionally, the diffuse emissions equatorward of the main emission and poleward of the satellite footprints are included as a fourth component (Bonfond et al., 2020). These components are physically distinct and generally vary independently of one another (Clarke et al., 2004), meaning each component may be considered separately. The most powerful of Jupiter's large-scale auroral forms, the auroral ME, forms two partially-closed ovals of vertically sheet-like aurorae around each of Jupiter's magnetic poles. In the southern hemisphere, the main emission appears superficially similar to Earth's auroral ovals, as Jupiter's southern magnetic pole is near its rotational axis (Connerney et al., 2018). In the north, the ME is warped into a kidney-bean shape due to an off-axis magnetic pole and the presence of a magnetic anomaly (Grodent et al., 2008), as illustrated in Figure

1. The auroral oval is always present and evolves slowly, on a timescale of tens of minutes, with intensities varying between $500 - 3000$ kiloRayleighs (kR) (Grodent et al., 2003; Clarke et al., 2004; Nichols et al., 2009). The auroral oval rotates with the planet, remaining fixed in planetocentric latitude and System III (SIII) longitude, the coordinate system referenced to the rotation of the Jovian magnetic field, in a state referred to as “corotation” (Gérard et al., 1994; Ballester et al., 1996; Clarke et al., 2004; Grodent, 2015). This is in direct contrast with the Earth’s aurorae, which form an oval largely fixed with the direction of the solar wind. Individual, small-scale (~ 1000 km wide) auroral features embedded in the main emission typically corotate as well (Gérard et al., 1994). Deviation from this motion is therefore interesting as it is indicative of an unusual magnetospheric process (Grodent, 2015). Deviations from corotation have been noted in the ME in the dusk sector (Grodent et al., 2003), near noon with the auroral discontinuity (Radioti et al., 2008) and noon auroral spot (Palmaerts et al., 2014), and in the dawn sector (Prangé et al., 1993; Ballester et al., 1996; Clarke et al., 1998; Gustin et al., 2006; Clarke et al., 2009; Nichols et al., 2009).

The ME owes its steadiness and motion to the corotation-enforcement field-aligned currents (FACs) coupling the magnetosphere and ionosphere, which have historically been identified as its dominant driver (Hill, 2001; Cowley & Bunce, 2001; Southwood & Kivelson, 2001). These currents map to the middle magnetosphere ($15 - 30$ R_J) where Iogenic plasma fills the magnetosphere and drifts outward, losing angular velocity in order to conserve angular momentum. The currents maintain the corotation of magnetospheric plasma by transferring angular momentum from the ionosphere to the plasma. They are strongestwhere the plasma angular velocity decreases most quickly, or where corotation begins to significantly breakdown, typically near $\sim$30 R_J (Hill, 2001). The electron precipitation associated with the upward currents excites atmospheric gas in the high latitude ionosphere, forming auroral emission; the strongest FACs form the ME (Cowley & Bunce, 2001). The FACs and resulting auroral emission are always present due to the continuous addition of new Iogenic plasma to the middle magnetosphere (Thomas et al., 2004), and are dominated by internal processes (Southwood & Kivelson, 2001) rather than external factors including the ambient solar wind (Clarke et al., 2009).

While the corotation-enforcement FACs are widely believed to dominate the Jovian main emission, not all of the predictions of this model have been borne out in in-situ measurements. While the *Juno* spacecraft has detected electron precipitation sufficient to power the main emission, it has also found equally or more powerful broadband, bi-directional electron acceleration to be common (Mauk et al., 2017, 2018, 2020). Acceleration processes other than the field-aligned potentials formed along FACs via the Knight relation (Knight, 1973) may be responsible for additional emission co-located with the main emission (Bonfond et al., 2020). Nonetheless, there is strong evidence that the main emission, at least in the dawn sector, is primarily driven by magnetosphere-ionosphere coupling FACs associated with corotation enforcement (Nichols & Cowley, 2022). Observations continue to support the overall picture of corotation-enforcement of outward drifting plasma, and by extension the corotation of the ME.

Jupiter’s enigmatic auroral dawn storms behave nearly opposite to typical auroral forms in the ME, despite appearing within the ME at local dawn. The dawn storms evolve over tens of minutes, reaching peak intensities $\gtrsim$3 MegaRayleighs (MR) in that time (Ballester et al., 1996; Gustin et al., 2006). From Earth-based observations the storms are also observed to significantly subcorotate, lagging behind rigid corotation by $\gtrsim$30% (Ballester et al., 1996; Gustin et al., 2006) and often remaining fixed entirely near local dawn (Clarke et al., 1998). These qualities define what we will refer to as “classical” dawn storms: brighter than average emission located near local dawn, with corotational velocity Ω along the ME of $0 \leq \Omega < 0.7\Omega_J$, where Ω_J is the rotation rate of Jupiter (i.e. $\Omega = \Omega_J$ denotes rigid corotation). In figure 1, an example of a classical dawn storm is compared to other features observed in the dawn sector of the main emission. Clas-

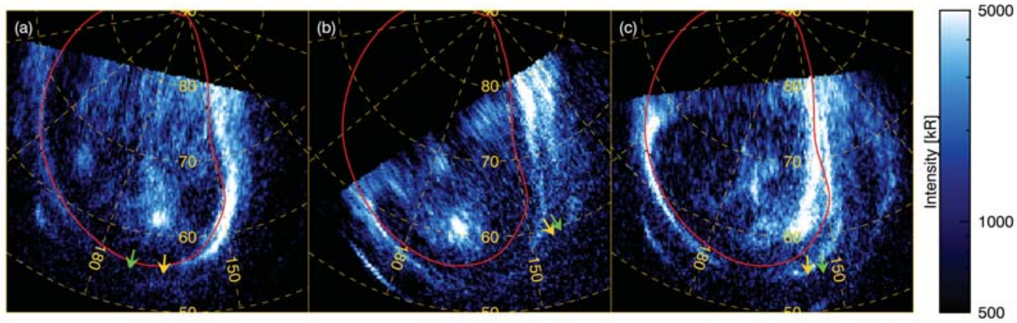

Figure 1. Example HST observations of the northern hemisphere main emission on three separate days (May 17, 2017, March 8, 2017, and March 21, 2017, respectively), with SIII longitude and latitude graticules plotted in yellow and the statistically-averaged location of the main emission in red. The direction to the Sun (yellow) and to the Earth (green) are marked with arrows; in all images, dawn is toward the left of the observation. Brightness in the image has been color-coded and log-scaled for clarity, corresponding to the colorbar on the right; brightness in these images has not been corrected for limb-brightening. Panel (a) shows dim (I=1540±150 kR), corotating (Ω=1.04±0.39Ω_J) emissions in the dawn sector; panel (b) shows brighter (I=3350±150 kR) and slightly subcorotating (Ω=0.76±0.20Ω_J) emissions near dawn; panel (c) shows the even brighter (I=4930±230 kR) and strongly subcorotating (Ω=0.32±0.05Ω_J) emissions near dawn. The dawn feature in (c) is a classical dawn storm. Brightness values have not been adjusted for limb-brightening, and are displayed with a log scale corresponding to the colorbar on the right.

sical dawn storms are rare, having been noted in ∼10% of archival observations (e.g. Prangé et al., 1993; Ballester et al., 1996; Clarke et al., 1998; Gustin et al., 2006; Clarke et al., 2009). Their subcorotational behavior is in stark contrast to the corotating main emission, and, while subcorotation is seen in the Earth's aurorae due to the dominance of the solar wind (e.g. Akasofu, 1981), is unexpected for emissions being driven by processes in Jupiter's middle magnetosphere (Southwood & Kivelson, 2001; Clarke et al., 2009), far from the solar wind boundary near 100 R_J (Joy et al., 2002). The intensity, fast evolution, rarity, and subcorotating motion of the classical dawn storms are unusual, considering the slowly-changing, always-present FACs thought to drive the ME emission.

The peculiarity of the dawn storms has gained wider attention since the arrival of NASA's *Juno* spacecraft at Jupiter. By comparing simultaneous HST observations with in-situ *Juno* measurements, Yao et al. (2020) found that a bright dawn emission observed with HST occurred shortly after *Juno* detected the signature of a magnetic reconnection event, and that further bright dawn emissions frequently coincided with plasma injection signatures in the aurorae. They concluded that reconnection was a likely driver of the emissions, with subsequent magnetic field dipolarization causing injection signatures. Similarly, Swithenbank-Harris et al. (2021) found dense, high-energy plasma with field-aligned motions in the middle magnetosphere, consistent with a reconnection event, at the same time as a very intense auroral form was observed in the dawn sector with HST. The feature they observe had a noonward leading edge which appeared to supercorotate at 2.5Ω_J. Using the *Juno* Ultraviolet Spectrograph (UVS) to observe Jupiter's nightside aurorae, Bonfond et al. (2021) found a sequence of auroral forms beginning near local midnight which precede bright dawn emissions, with either the final auroral forms as a whole (in dim cases) or their leading edge (in bright cases) accelerating toward corotation as they approach dawn, then apparently corotating after. They find dawn-storm-like emission in approximately half of the first 20 *Juno* perijoves, far exceeding the ∼10% occurrence rate found through HST observations. By comparing the sequence of auroral forms to similar forms observed in terrestrial aurorae, they concluded that these emissions are likely related to reconnection and dipolarization. Taken together, these results suggest some correlation between bright auroral features near dawn and magnetic reconnection, dipolarization, and injection signatures. It is important to note that the auroral features identified in these studies are not required to be subcorotating, and thus often are not classical dawn storms.

Both the corotation-enforcement theory and the *Juno*-based findings are in tension with the observed behaviors of classical dawn storms. While simple, axisymmetric corotation-enforcement theory cannot explain the behavior of subcorotating features by definition, modeled FACs tend to peak near where the plasma angular velocity is $\sim 0.9\Omega_J$ (Hill, 2001; Cowley & Bunce, 2001; Nichols et al., 2020), which serves as a reasonable estimate for the rotation rate of auroral features associated with the FACs and is in keeping with observations (Grodent, 2015). The recent *Juno* results show that emissions frequently form with a trailing edge effectively fixed at midnight and a leading edge corotating or super-corotating toward noon through the dawn sector, equivalently having a center-of-brightness corotation rate of $0.5\Omega_J \lesssim \Omega \lesssim 1.25\Omega_J$ (Swithenbank-Harris et al., 2021; Bonfond et al., 2021). Classical dawn storms, however, are expected to move with corotation rates of $0 \lesssim \Omega \lesssim 0.7\Omega_J$ (Clarke et al., 2009).

To quantify the significance of this tension and develop a complete picture of the formation and evolution of classical dawn storms, the properties of dawn storms, other auroral forms in the dawn sector, and auroral forms outside of the dawn sector must be carefully measured. Changes to the intensity, location, morphology, and behaviors of ME auroral forms are reflections of the magnetospheric processes which drive them. By measuring these properties remotely using Hubble Space Telescope (HST) observations of the ME, the structure and dynamics of the Jovian middle magnetosphere can be measured. Perturbations to the steady-state main emission must correlate to atypical magnetospheric process occurring in the region of the middle magnetosphere mapping to those emissions along magnetic field lines (Grodent, 2015). Processes known to perturb the ME include solar wind compressions (Waite et al., 2001; Kita et al., 2016), the geometry of Jupiter's magnetic field (Kimura et al., 2017), volcanic events on Io (Bonfond et al., 2012; Kimura et al., 2018), and local time effects (Tao et al., 2010; Ray et al., 2014). In this paper, we identify hundreds of auroral features in the dayside main emission in the first survey of Jupiter's aurorae to systematically measure corotation rate. With this survey, we quantify the difference in corotational behavior between dawn storms and other ME auroral features, both inside and outside of the dawn sector. A statistical survey of this scale can only be carried out using the wealth of archival HST observations available.

2 Observations

The set of HST images analyzed here comprises 1518 Advanced Camera for Surveys Solar Blind Channel (ACS/SBC) observations and 252 Space Telescope Imaging Spectrograph (STIS) observations of the Jovian FUV aurorae spanning over 12 years. Earlier Wide Field and Planetary Camera 2 (WFPC2) images had lower resolution and sensitivity and are not included. Approximately 80% of the observations used were of Jupiter's northern aurorae, with the remaining 20% of the southern aurorae. The ACS observations are ∼100 s integrations in the accumulated imaging mode using either the F115LP or F125LP filters covering nearly every day in a 52 day span in 2007 (see Clarke et al. (2009) for details). The STIS observations are ∼40 min. integrations in the time-tagged imaging mode of the Far Ultraviolet-Multi-Anode Microchannel Array (FUV-MAMA) using the F25SRF2 filter contemporaneous with perijoves of NASA's *Juno* spacecraft (see

Nichols et al. (2017) and Grodent et al. (2018) for details). These observations track Jupiter from 2016-2019 covering roughly a quarter of a Jovian year. Key details of these observing campaigns are included in Table 1.

Table 1. HST Observations

Program	Start date	End date	Configuration	Cumulative exposure time (hours)
GO 10862	Feb. 20 2007	Jun. 11 2007	ACS/SBC	42[a]
GO 14105	May 16 2016	Jul. 18 2016	STIS/FUV-MAMA	35
GO 14634	Nov. 30 2016	May 23 2018	STIS/FUV-MAMA	101
GO 15638	Feb. 9 2019	Sep. 13 2019	STIS/FUV-MAMA	36

[a]Only orbits dedicated to observing Jupiter are included.

Images were extracted from the time-tagged observations by integrating over non-overlapping 30 s intervals of each exposure; the accumulated ACS images were unchanged. All images were reduced using the custom Boston University HST data reduction pipeline, which performs dark count subtraction, flat fielding, interpolation over bad anode rows where applicable, and corrects for geometric distortion using the most recent reference files available, as previously documented (e.g. Clarke et al., 2009; Nichols et al., 2009). Intensities were converted from counts/s to kiloRayeligh s (kR) of unabsorbed H and H_2 emission using the conversion factors of Gustin et al. (2012) and assuming a color ratio of 2.5. The intensities of the ACS observations were uniformly enhanced by a factor of 1.4 for those using the F115LP filter and 1.6 for those using the F125LP filter following the reanalysis of the absolute flux calibration of the SBC (Avila et al., 2019).

The center of the disk of the planet was determined by fitting a simulated planetary disk to the image manually, introducing a conservative error of 5 pixels in both the horizontal and vertical, equivalent to $\sim$370 km or $\sim 0.3°$ near the equator. The images were rotated such that the rotational north pole is vertical and near the top of the image; the images were scaled to account for changes in the observing geometry using NASA Navigation and Ancillary Information Facility (NAIF) ephemerides (Acton et al., 2018). The geocoronal background was accounted for by subtracting the mean value of a $500\times$ 100 pixel region of sky far from the planetary limb. The Rayleigh-scattered solar continuum emission of the Jovian disk was modeled as a latitudinal band profile averaged over all the observations within a single observing program, and was subtracted from each observation. Remaining large-scale brightness variations were subtracted using a modified Minnaert function following Vincent et al. (2000); the small amount of Jupiter's disk in most images did not allow a third-order form to be fit uniformly, so a first-order Minnaert function was used instead. Reduced images were projected onto planetocentric, equirectangular maps.

3 Methods

3.1 Keogram Creation

The keograms constructed here are two-dimensional representations of the evolution of the ME emission over an entire HST visit; similar keograms have been previously used effectively at Jupiter to identify new auroral emissions (e.g. Nichols et al., 2017). In each keogram, a single observation, or sub-integrated image in the case of time-tagged STIS observations, corresponds to a horizontal, one-dimensional profile of ME brightness. The ME brightness is extracted from an image by first linearizing a 6° region perpendicular to and centered on the statistically-averaged location of the ME (or "statis-

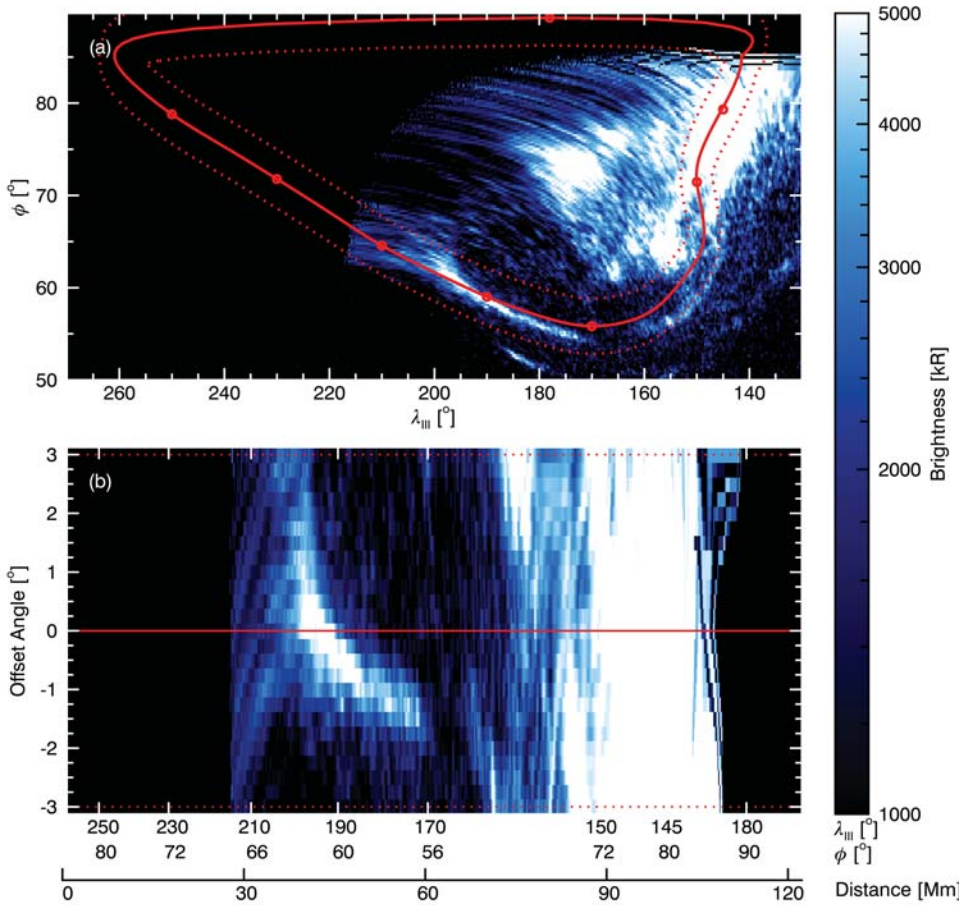

Figure 2. Maps of the northern ME from March 21, 2017, from the same observations as Figure 1c, showing (a) the northern ME on an equirectangular grid with the statistical main oval (solid red line) and the oval offset perpendicularly by ±3° (red dotted lines) overplotted, and (b) the same after linearizing along the statistical main oval, with equivalent lines. Longitude (λ_{III}) and latitude (ϕ) labels in (b) correspond to the locations marked with red circles in (a), and (b) is additionally labeled with the distance along the statistical main oval starting at the point nearest local midnight in Megameters (Mm). Brightnesses are not adjusted for limb-brightening and are log-scaled for clarity, corresponding to the colorbar on the right.

tical main oval") described by Nichols et al. (2009). This region was binned such that distance along the statistical main oval increases linearly along the x-axis. Each pixel of the image therefore measures the same physical distance in Jupiter's atmosphere horizontally, as illustrated in Figure 2. The brightness profile is obtained by taking the average of the fourth (highest) quartile of intensities measured in that bin as a representative brightness. The brightest values in the each bin generally belong to the ME, and taking the brightness of these points regardless of where they occur on the vertical axis allows the ME to be sampled while allowing for potential deviations of up to ±3° latitude from the statistical main oval used (Grodent et al., 2008).

One-dimensional brightness profiles were produced for all exposures or sub-integrations within the same HST visit. Successive profiles were vertically stacked below the preceding profile to build up the keogram. The resulting keogram is a two dimensional image with location along the statistical main oval measured horizontally, increasing rightward, and time measured vertically, increasing downward, as illustrated in Figure 3. The horizontal axis of the keograms was binned such that each unit corresponds to a fixed distance measured along the statistical main oval, beginning at the corotating point closest to local midnight at the beginning of the observation. Distance along the main oval is a useful measure since it strictly increases along both the north and south main ovals, unlike longitude or latitude, and preserves the apparent scale of the emission feature, unlike local time. As distance along the statistical main oval is not a physically relevant measure, the horizontal axes are labelled with the corresponding SIII longitude (λ_{III}) and latitude (ϕ) on the lower axis and local times (LT) on the upper axis. The keograms are in Jupiter's rotating reference frame. Corotating features appear as vertical lines on the keograms, subcorotating features appear to slope leftward with increasing time, and super-corotating features would appear to slope rightward.

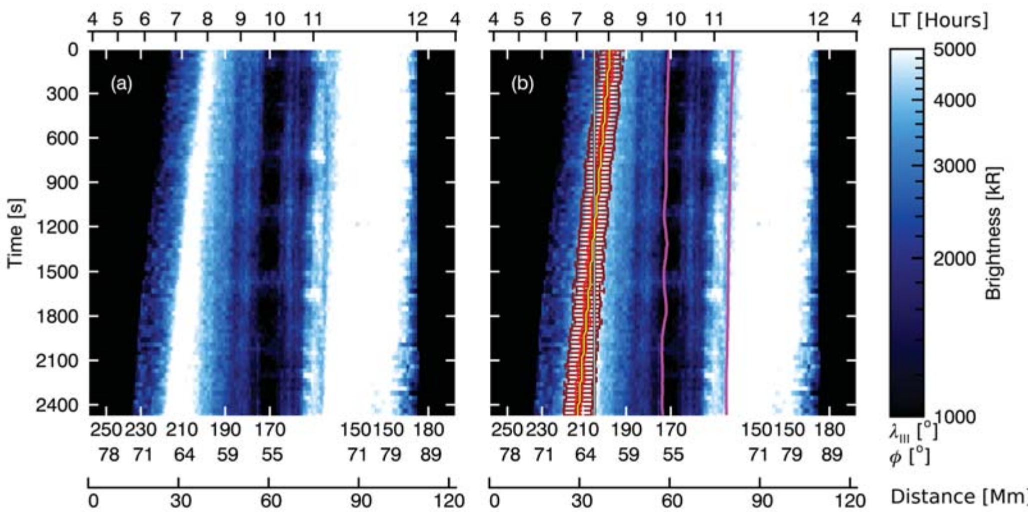

Figure 3. Keograms– two-dimensional space-time plots created to more easily identify main emission features and characterize their properties, including corotation rates– shown for the same March 21, 2017 observation as Figures 1c and 2. Here, the same keogram is shown without any overlays (a) and with overlays (b) for: the feature identification boundaries (magenta lines), a subcorotating dawn storm's center-of-brightness (red circles) with errors (dark red capped bars), a reference line for $\Omega = 0$ (yellow line), and a reference line for $\Omega = \Omega_J$ (gray line). The intensities are not adjusted for limb-brightening and are log-scaled, corresponding to the colorbar on the right. The horizontal axes measure System III longitude (λ_{III}) and latitude (ϕ) in degrees, distance along the ME in Mm, and local time (LT) in hours.

3.2 Auroral Feature Identification

For this study, auroral features were defined as regions of high intensity spanning the entire exposure, or vertical range, of the keogram. Features were automatically identified to prevent selection bias. First, a brightness profile summed over time was found and smoothed; the local maxima of this profile were used as initial, approximate horizontal locations of auroral features. This approximation is valid as non-corotating auroral features move slowly relative to the planet's rotation. Boundaries between these approximate locations were then found as the contour of lowest, constant intensity spanning the entire vertical range of the keogram after applying a low-pass filter. An example of the resulting boundaries is shown in Figure 3b. If a contour matching these parameters could not be created between two neighboring maxima, then the two maxima were considered to belong to the same feature. Emissions lying between boundaries, or between the edge of the keogram and a boundary, were identified as auroral features.

3.3 Measurement of Auroral Feature Properties

For each auroral feature, the brightness and position between each set of boundaries and in each vertical bin were then found. Emission features were fit with Chebyshev's inequality, which was used to find the smallest region containing 25% and 50% of the total emission in that brightness profile. The center of the former was chosen to represent the center-of-brightness of the feature and the bounds of the latter range represent $2\sqrt{2}\sigma$ errors on the center-of-brightness. The characteristic brightness of the feature was found as the mean brightness contained within the smallest range containing 25% of the total emission. This method was preferred over fitting a Gaussian to each feature as it gives a robust estimate of the location without requiring any particular shape in the brightness profile. Features for which the majority the 2σ errors corresponded to the planetary limb, the edge of the observation, or the far side of the planet were excluded from the analysis.

Corotation rates Ω, varying between 0 for features perfectly fixed in local time and Ω_J for features fixed in planetocentric coordinates, or corotating, were found for every identified feature by the relation

$$\Omega = \left(1 - \frac{1}{N_{obs} - 2} \sum_{n=1}^{N_{obs}-1} \frac{m_{C,n}}{m_{LT,n}}\right) \Omega_J \tag{1}$$

where $m_{C,n}$ represents the slope of the center-of-brightness of a feature in the keogram in the n-th exposure, $m_{LT,n}$ is that of constant local time, and N_{obs} is the number of exposures making up the keogram. As neither the north nor south main ovals are a perfect circle, the rate at which local time passes along the main oval changes as a function of location on the planet. This nonlinear effect is accounted for by measuring the slopes in each observation or sub-integration and averaging the ratio of these together before finding an overall corotation rate Ω. Slopes are not found for the first and last exposures, so the total number of slopes is two less than the number of observations N_{obs}. Local time along the main oval is calculated as the hour angle, in System III longitude, of the emission feature relative to local noon, which is set to the central meridian longitude of the Sun (CMLS) in the observation. An example of the feature identification, with reference lines indicating $\Omega = \Omega_J$ and $\Omega = 0$ overplotted, is shown in Figure 3b. Rotation rates are measured relative to Jupiter's rotation and local time in the ionosphere; magnetospheric processes driving these emissions may not exactly match the rotation rate of their corresponding auroral emissions, due to variation in the magnetic field. Non-physical corotation rates resulting from poor measurement of a feature's center-of-brightness, defined as measured corotation rates with either a 3σ lower limit $> 1.5\Omega_J$ or a 3σ upper limit < 0, are excluded from the analysis. It is important to note that corotation rates are based on the apparent motion of the center-of-brightness of the emission feature parallel to the reference statistical main oval. The corotation rates reported here do not necessarily reflect the apparent motion of the leading or trailing edge of the feature, nor do they account for any apparent motion perpendicular to the statistical main oval. Motion perpendicular to the statistical main oval may arise from a misalignment of the statistical main oval with the ME; for misalignments of $\sim 3°$, the measured corotation rate would change by 0.1%. Subcorotating emission features may have corotating or super corotating leading edges.

3.4 Application of Limb-Brightening Correction

All earth-based observations of Jupiter's aurorae are affected by limb-brightening, this analysis included. Due to the observing geometry, the dawn terminator is always near the limb of the planet, and thus subject to large limb-brightening effects. While limb-brightening has a significant effect on the measured intensities of the auroral emissions near dawn, it is not expected to seriously affect the feature identification algorithm or the measurement of feature positions and corotation rates, as these are based strictly on the relative brightness of neighboring segments of the main emission. For these measurements, we propagate the effects of a simple model of limb-brightening as an additional source of error, with minor effect compared to other sources of error. We report the brightness of each feature both with and without the full limb-brightening correction.

We estimate the limb-brightening factor at all points along the reference oval as the inverse cosine of the view angle (Grodent et al., 2005), analogous to the air mass correction for astronomical observations. The limb-brightening factor is thus generally overestimated at large angles, tending toward infinity near the edge of the disk of the planet rather than the expected factor of a few tens (Grodent et al., 1997). The measured brightness along the reference oval is then divided by the corresponding limb-brightening factors to yield a corrected version of the emission profile. The limb-brightening correction shifts the peaks of the emission slightly. The center-of-brightness of each feature in the limb-brightening-corrected keogram is estimated by finding the nearest maximum to the original center-of-brightness after the corrected profile has been smoothed with a box-car of width $\sim$3% the keogram width. As it is constrained by the position of the center-of-brightness in the uncorrected image, the maximum is a useful estimate of the center-of-brightness in the corrected image. Finding the corrected center-of-brightness in this way potentially overestimates the shift from the original, but allows for fast limb-brightening correction while contributing to the robustness of our error estimation. This shift in center-of-brightness does not directly correspond to a change in the measured corotation rates, which is related to the slope of the line connecting the center-of-brightness points rather than their absolute positions. The change to the slopes, and therefore the corotation rates, that the limb-brightening correction causes can be understood as an additional source of uncertainty to the original corotation rate measurements. The local slope of the line connecting the corrected centers-of-brightness is measured for each point, the typical difference between the corrected slopes and the original slopes is calculated, and that difference is propagated through Equation 1 as a source of error. The final change in the error can be found by the difference of the original error and the root-sum-square of the original error and the new error; the mean change in the error is $\sim$0.05. We find that limb-brightening correction is not a significant source of error for these measurements, as 0.05 is significantly less than the propagated error in the planet center pixel and the mean error of the feature corotation rates ($\sim 0.2\Omega_J$).

Correcting for limb-brightening has a more significant impact on the distribution of feature intensities across the ME. This is due to the very large limb-brightening correction factors we use near the dawn limb, as the dawn sector is always near the limb where the correction factors grow toward infinity. Due to typical observing conditions, feature brightness in the noon and dusk sectors is not affected as greatly as that in the dawn sector, as the noon and dusk sectors of the statistical main oval in the northern hemisphere are farther from the limb of the planet. We note that the extreme limb-brightening correction near dawn is a limitation of the simple model of limb-brightening we use rather than being physical, and as such we present both the corrected and uncorrected brightnesses. All figures are presented with uncorrected brightness values.

4 Results

The corotation rates of auroral emission features, split into those originating in the dawn sector (3-9 LT) and elsewhere (0-3 LT, 9-24 LT), are shown in Figure 4. As these are Earth-based observations, only $\sim$6−18 LT were observable. After removing features detected near the edges of the keogram and those with nonphysical corotation rates, as described previously, 734 total features were detected: 281 in the dawn sector and 453 elsewhere. Features outside of the dawn sector follow a narrow distribution of corotation rates, with $\sim$63% of ME features outside of dawn falling between $0.8\Omega_J < \Omega < 1.1\Omega_J$ and 91% falling between $0 < \Omega < 1.25\Omega_J$. This corotational behavior reflects the motion of the ME as a whole. Owing to the reported rarity of the classical dawn storms, we expected the distribution of corotation rates for dawn sector features to be similar to that for other sectors, with a small increase near zero from the contribution of the dawn storms. In contrast, we find evidence of widespread subcorotation in the dawn sector, as demonstrated in Figure 4. Dawn sector features have a broad distribution of corotation rates, with 42% falling between $0 < \Omega < 0.8\Omega_J$, 32% falling between $0.8 < \Omega < 1.1\Omega_J$, and 82% falling between $0 < \Omega < 1.25\Omega_J$. Dawn features are overrepresented compared to non-dawn features at all corotation rates less than $0.8\Omega_J$. We will call features subcorotating with $\Omega < 0.8\Omega_J$ "significantly subcorotating" from this point; 42% of the dawn features identified here significantly subcorotate. The $0.8\Omega_J$ corotation rate cutoff is similar to previous values used to characterize dawn storms (Ballester et al., 1996). The results do not depend on this value; it is only chosen to make further discussion clearer. The observed distribution of corotation rates in the dawn sector is highly unlikely to be drawn from the same underlying population as the distribution in other sectors, as confirmed by a KS-test at a significance level $\alpha < 0.001$ (i.e. $> 99.9\%$ confidence). Probability densities are continuous and take measurement errors into account, with the densities integrated over fixed-width intervals to create histograms.

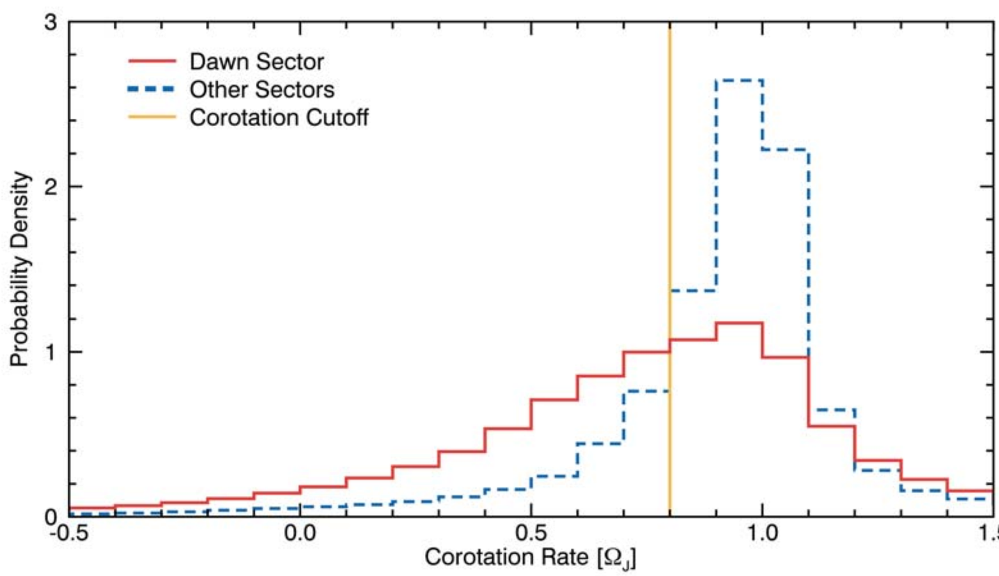

Figure 4. Histograms showing the probability density distribution of corotation rates of ME auroral features. The black, dashed line shows features which began outside the dawn sector, while the red line shows features which began in the dawn sector. Dawn features are overrepresented at corotation rates less than $0.8\Omega_J$ and underrepresented at higher corotation rates.

Classical dawn storms have also been consistently characterized as more intense than typical of the ME. If all of these significantly subcorotating emissions identified in the dawn sector were classical dawn storms, we would expect these features to be similarly overrepresented at high intensities. As illustrated in Figure 5a, this is not the case: the brightness distributions for dawn sector features and non-dawn sector features are very similar, with non-dawn sector features slightly more likely at higher intensities. Both distributions are broadly peaked, with 92% of dawn features and 90% of non-dawn features having intensities between 0.5 MR $< I \leq 6$ MR before correcting for limb-brightening. The two distributions are different at a significance level $\alpha < 0.05$ (95% confidence). We note that the brightness values shown here are representative of the feature center-of-brightness rather than the bulk ME brightness, and so are expected to be higher than the average brightness of the main emission separate from the effects of limb-brightening. For the same reasons, this result is not in conflict with previous findings that the dawn ME is typically dimmer than the dusk ME(Bonfond et al., 2015). The limb-brightening correction used here reduces the intensities of emissions near the limb of the planet more than is physical, so the overabundance of dawn features in Figure 5b between $0-500$ kR compared to features in other sectors is expected. This overabundance inflates the difference between the distributions, leading to a significance level $\alpha < 0.001$ (99.9% confidence) that the two distributions are different. More insight is gained by instead looking at the correlation between auroral feature corotation rate and intensity in the dawn sector, which should be both strong and negative if all significantly subcorotating emissions were bright classical dawn storms. We find no significant correlation between corotation rate and brightness in the dawn sector (Pearson correlation coefficient $r = 0.03$ before limb-brightening correction and $r = 0.21$ after).

Dim, subcorotating auroral features must appear frequently in the dawn sector ME to explain the clear dichotomy between dawn and the rest of the ME in corotation rate, as shown in Figure 4, and the similarity between the two regions in mean intensity, as shown in Figure 5. Subcorotation in the dawn sector must either not be unique to classical dawn storms, or classical dawn storms must be far more common and dimmer than previously expected. The ~12 year span of our survey strongly supports the idea that significantly subcorotating emissions are common in the dawn sector of Jupiter's ME aurorae, which suggests the underlying physics driving these emissions must be similarly common.

5 Discussion

We have identified hundreds of auroral features in Jupiter's dayside main auroral emission and have systematically measured their positions in local time, corotation rates, and intensities, allowing the comparison of large distributions of these properties for the first time. We are thus able to compare the properties of classical dawn storms to the typical properties of auroral forms both inside and outside the dawn sector. We are specifically interested in the distributions of corotation rates in the dawn sector and other sectors, and how these distributions compare to the corotation rates associated with classical dawn storms. This comparison is needed to understand the physical processes driving the dawn storms.

Classical dawn storms have been observed to subcorotate with corotation rates between $0 \lesssim \Omega < 0.7\Omega_J$ (Ballester et al., 1996; Clarke et al., 1998; Gustin et al., 2006). Over 50% of the auroral features we identify in the dawn sector have corotation rates in this range; they do not all, however, have the elevated brightness of a classical dawn storms. Instead, the brightnesses of features in the dawn sector have a similar distribution to features elsewhere in the ME. Further, while classical dawn storms are rare, occurring in just ~10% of observations, these subcorotating emissions are commonly observed. From these observations it appears that the causes of the subcorotation and high intensities of the dawn storms, while traditionally assumed to be related, if not identi-

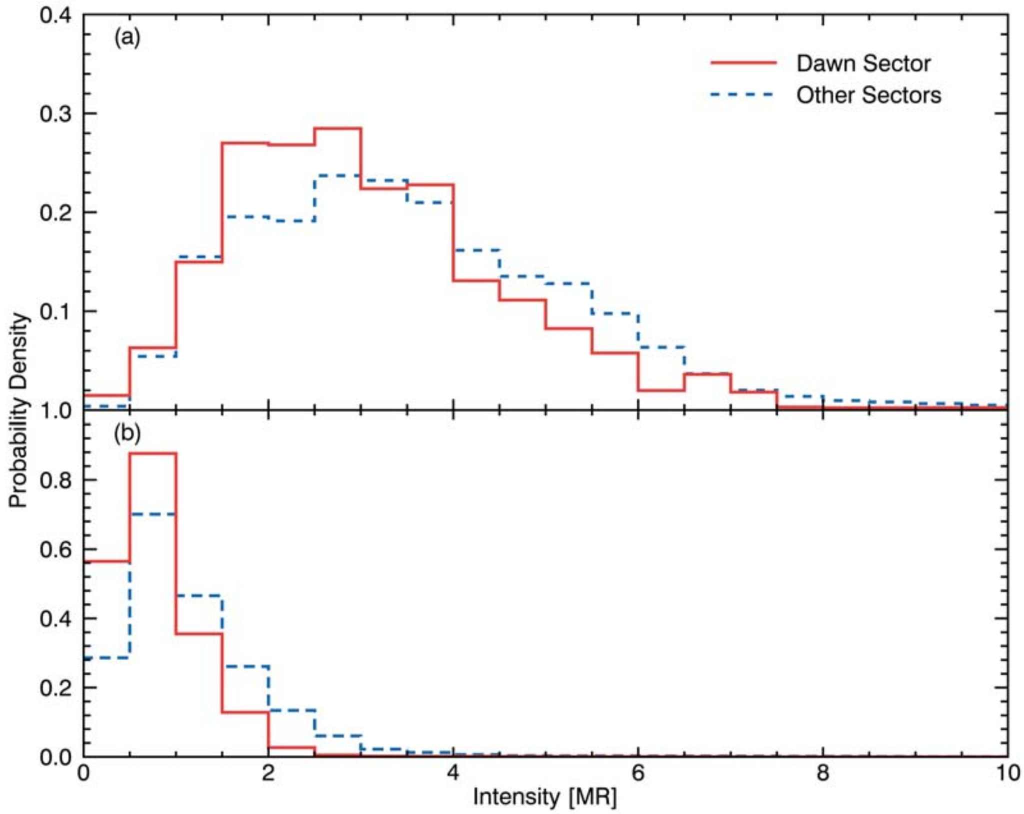

Figure 5. Histograms showing the probability density distribution for the mean intensities of ME features in HST observations. Blue, dashed lines show features which began outside the dawn sector, while red lines show features which began in the dawn sector. Panel (a) shows the distributions before correcting for limb-brightening. Roughly 90% of dawn features and non-dawn features have intensities between 0.5 MR and 6 MR. There is no statistically significant difference in the two distributions. Panel (b) shows the distributions after correcting for limb-brightening. The distributions appear slightly more distinct, but this is partially due to the extreme, non-physical correction applied near the dawn limb.

cal, are in fact unrelated. Subcorotation occurs in the dawn sector far more often than elsewhere in the ME region, and is not correlated with the intensities of the associated auroral forms.

Approximately 30% of the auroral features observed in the dawn sector corotate with $0.8\Omega_J \lesssim \Omega < 1.1\Omega_J$. This range, where the distribution of non-dawn features peaks, may be associated with auroral features primarily generated by corotation-enforcement currents, which are maximized when magnetospheric plasma has an angular velocity of $\sim 0.9\Omega_J$ (Hill, 2001; Cowley & Bunce, 2001; Nichols et al., 2020). Near 65% of dawn features are potentially consistent with begin driven by magnetic reconnection, with corotation rates of $0.5\Omega_J \leq \Omega < 1.25\Omega_J$. From this observational study, we can not distinguish between these two theories in the range $0.8\Omega_J \leq \Omega < 1.1\Omega_J$. If we assume all auroral features in that range are the result of the corotation enforcement FACs, we may very roughly estimate a lower bound in the occurrence rate of magnetic-reconnection-driven dawn auroral forms of $65\% - 30\% \approx 35\%$. This lower bound does not take the intensities of the auroral features into consideration, and so this $35 - 65\%$ range may be compared to the ∼50% occurrence rate of dawn-storm-like events identified by Bonfond et al. (2021). Neither corotation-enforcement theory nor the magnetic reconnection theory predict the ∼25% of features lagging behind corotation by more than 50%.

We propose that the unexplained subcorotational behavior identified in some auroral features may be consistent with corotation enforcement theory after accounting for Jupiter's variable ionospheric conductance. The conductance of Jupiter's ionosphere is broadly modulated by the photoionoization of neutral atoms from incident solar extreme ultraviolet (EUV) light (Tao et al., 2010) and locally by particle precipitation, as demonstrated both theoretically (Millward et al., 2002) and observationally (Gérard et al., 2020). The conductance is typically dominated by particle precipitation near the aurorae, but the contribution from solar EUV may play a major role near the dawn terminator. Here, the ME is typically dimmer than elsewhere (Bonfond et al., 2015) and has a correspondingly smaller contribution to the conductance (Millward et al., 2002). In the same location, the conductance due to incident solar EUV jumps by nearly an order of magnitude over ∼1 hour local time where the previously unlit ionosphere suddenly experiences incident solar EUV flux again, bringing the solar-driven contribution to the conductance within an order of magnitude of the aurora-driven contribution for dim (∼100 kR) auroral emissions (Millward et al., 2002; Tao et al., 2010). Further, there is an enhancement in subcorotating plasma just before dawn and a corresponding acceleration of plasma-laden flux tubes up to, or beyond, corotational velocities according to both in-situ measurements (Krupp et al., 2001) and models (Chané et al., 2017). The acceleration of flux tubes must be accomplished by corotation-enforcement FACs (Nichols & Cowley, 2022), which further suggests the presence of strong currents fixed to the dawn sector. FACs reach their absolute highest values near dawn in quasi-azimuthally symmetric models of Jupiter's field-aligned current system (Ray et al., 2014), and have a local maximum near dawn in non-azimuthally symmetric models (Chané et al., 2018) and in-site measurements (Lorch et al., 2020).

Combined, these factors make the dawn sector a likely location to host subcorotating emissions. The increase in conductance at dawn allows the ionosphere to suddenly support larger currents, while the presence of subcorotating magnetospheric plasma drives current formation. An increase in EUV-driven conductance and subcorotating-plasma-driven currents would further enhance the conductance via electron precipitation and collision. As the corotation enforcement currents near dawn grows larger, they will tend to dominate the local conductance again. In this scenario, the increase in the dawn conductance due to solar EUV serves as a small perturbation to allow the currents to grow. We note that a localized conductance increase near local dawn may occur in some of the ionospheric Pedersen conductances calculated by Gérard et al. (2020), though without characterizing the scale of this process it is difficult to predict how it should manifest in such maps. As this enhanced conductance is unique to dawn, the resulting auroral features should appear to significantly subcorotate, remaining fixed near dawn while the magnetospheric plasma and ionosphere rotate with the planet through the dawn region. Testing specific predictions of this theory is outside the scope of this observational paper; a statistical analysis of in-situ magnetospheric plasma velocities and currents near local dawn, combined with comparisons to auroral intensities and behavior, is needed to further explore it.

Invoking the effects of solar EUV in driving dawn-fixed auroral emissions like the dawn storms is conceptually similar to previous theories which connected dawn storms with variations in the solar wind. Both attempt to explain this motion, in which features are fixed relative to the Sun-Jupiter geometry, with properties relating to the Sun rather than Jupiter. A connection between the solar wind and the dawn storms has, however, never been found (Clarke et al., 2009; Nichols et al., 2009) and would be theoretically difficult to explain, as any solar wind disturbance would have to propagate into the middle magnetosphere at ∼20 R_J from the magnetopause near 100 R_J (Joy et al., 2002).

The theory we present does not have this problem as changes in the solar EUV flux propagate through the magnetosphere unimpeded by magnetic field lines. For fixed solar conditions, the ionospheric ionization due to solar EUV is constant at any given local time.

The theory we present here specifically addresses the behaviors of dawn auroral features, and is compatible with the driving of bright auroral events by both corotation enforcement currents and magnetic reconnection and dipolarization. Magnetic reconnection events, or other irregularities in the distribution of the plasma in the middle magnetosphere, may explain the intermittent nature of dawn-fixed auroral features. Plasma injection into the dawn sector magnetosphere following reconnection events may trigger intense emissions, while the ionospheric conductance modulates the corotation rates of such features. The process we describe is compatible with recent observations and theory linking the dawn storms to magnetic reconnection (Yao et al., 2020; Swithenbank-Harris et al., 2021; Bonfond et al., 2021). Other variations in the distribution of plasma in the middle magnetosphere, such as the spiral-shaped distribution modeled by Chané et al. (2017), could also explain the sporadic nature of the dawn-fixed features we have identified.

Finally, we note that we cannot differentiate between drivers of dawn sector auroral forms where the expected corotation rate distributions overlap. We find that $< 20\%$ of dawn features corotate in keeping with the simple picture of corotation-enforcement FACs, and that $\sim$65% are consistent with the expected results of magnetic reconnection. The prominence of magnetic reconnection driven aurorae is uncertain (Nichols & Cowley, 2022), and reconnection may be too rare to fully explain the $\sim$45% of features attributed solely to it. Instead, many more ($\lesssim$60%) features may be consistent with the schematic of corotation-enforcement with solar EUV modulated ionospheric conductance previously outlined here; at a minimum, $\sim$25% of auroral forms can be explained by this theory. Despite the multitude of physical drivers influencing the motions of auroral forms in the dawn sector, the motions of auroral features in the noon and dusk sectors are consistent with the accepted corotation-enforcement current theory.

6 Conclusions

We have shown that nearly half of all auroral features in the dawn sector significantly subcorotate, lagging behind rigid corotation by $\gtrsim 20\%$ ($0 < \Omega \leq 0.8\Omega_J$). This behavior is distinct from that of features outside the dawn sector, which corotate the majority of the time. The high prevalence of subcorotation in the dawn sector is unexpected and indicates that the physical drivers of this behavior in auroral forms are common, not unique to the rare dawn storms as previously expected. Rare magnetospheric phenomena which have previously been investigated as potential drivers of the dawn storms, such as events in the solar wind, cannot be invoked to explain the motions of the features. Instead, it is better to characterize the dawn storms as one aspect of a far more common auroral phenomenon occurring at dawn, which sheds new light on the physics behind both the storms and the widespread significant subcorotation of dawn aurorae. We find a wide range of corotation rates among dawn sector auroral forms: $\sim$20% of features are consistent with the rigid corotation expected from a simple model of corotation-enforcement FACs, and $\sim$65% are consistent with the corotational behavior associated with magnetic reconnection events. The 25% of features inconsistent with both of these models, those that remain nearly fixed near dawn ($0 < \Omega \leq 0.5\Omega_J$), are newly identified here. Their significant subcorotation may be controlled by increased ionospheric conductance, subcorotating magnetospheric plasma, and the field-aligned currents associated with both; these physical mechanisms are unique to the dawn sector, and support significant subcorotation. This proposed process is a slight modification to the typical corotation-enforcement model widely accepted to drive the bulk of Jupiter's main emission, and is compatible with both the simple corotation-enforcement model and the magnetic reconnection model. Future investigations into the motions of auroral forms should compare directly to in-situ measurements of plasma in the middle magnetosphere or to models of the corotation-enforcement current system which include variable ionospheric conductance in order to more fully explore the theory presented here.

Acknowledgments

The authors would like to thank Dr. Denis Grodent, both for a portion of the HST observations used in this analysis and for valuable commentary on the direction of the paper. This work is based on observations with the NASA/ESA Hubble Space Telescope, obtained from the Mikulski Archive for Space Telescopes (MAST) at the Space Telescope Science Institute (STScI). STScI is operated by the Association of Universities for Research in Astronomy, Inc., under NASA contract NAS5-26555. This work was supported by STScI awards HST-GO-16193.002-A and HST-GO-16195.002-A and in part by the Massachusetts Space Grant Consortium (MASGC).

Data Availability Statement

The HST image data used in this analysis are available at the MAST archive hosted by the STScI, either by searching the program IDs or via doi 10.17909/ekt0-mf55.

References

Acton, C., Bachman, N., Semenov, B., & Wright, E. (2018). A look towards the future in the handling of space science mission geometry. *Planetary and Space Science*, *150*, 9-12. Retrieved from `https://www.sciencedirect.com/science/article/pii/S0032063316303129` (Enabling Open and Interoperable Access to Planetary Science and Heliophysics Databases and Tools) doi: https://doi.org/10.1016/j.pss.2017.02.013

Akasofu, S. I. (1981, June). Energy coupling between the solar wind and the magnetosphere. *Space Science Reviews*, *28*(2), 121-190. doi: 10.1007/BF00218810

Avila, R. J., Bohlin, R., Hathi, N., Lockwood, S., Lim, P. L., & De La Pena, M. (2019, October). *SBC Absolute Flux Calibration.* Instrument Science Report ACS 2019-5.

Ballester, G. E., Clarke, J. T., Trauger, J. T., Harris, W. M., Stapelfeldt, K. R., Crisp, D., ... Westphal, J. A. (1996). Time-resolved observations of jupiter's far-ultraviolet aurora. *Science*, *274*(5286), 409–413. Retrieved from `https://science.sciencemag.org/content/274/5286/409` doi: 10.1126/science.274.5286.409

Bonfond, B., Grodent, D., Gérard, J. C., Stallard, T., Clarke, J. T., Yoneda, M., ... Gustin, J. (2012, January). Auroral evidence of Io's control over the magnetosphere of Jupiter. *Geophysical Research Letters*, *39*(1), L01105. doi: 10.1029/2011GL050253

Bonfond, B., Gustin, J., Gérard, J. C., Grodent, D., Radioti, A., Palmaerts, B., ... Tao, C. (2015, October). The far-ultraviolet main auroral emission at Jupiter - Part 1: Dawn-dusk brightness asymmetries. *Annales Geophysicae*, *33*(10), 1203-1209. doi: 10.5194/angeo-33-1203-2015

Bonfond, B., Yao, Z., & Grodent, D. (2020). Six pieces of evidence against the corotation enforcement theory to explain the main aurora at jupiter. *Journal of Geophysical Research: Space Physics*, *125*(11), e2020JA028152. Retrieved from `https://agupubs.onlinelibrary.wiley.com/doi/abs/10.1029/2020JA028152` (e2020JA028152 10.1029/2020JA028152) doi: https://doi.org/10.1029/2020JA028152

Bonfond, B., Yao, Z. H., Gladstone, G. R., Grodent, D., Gérard, J.-C., Matar, J., ... Bolton, S. J. (2021). Are dawn storms jupiter's auroral substorms? *AGU Advances*, *2*(1), e2020AV000275. Retrieved from `https://`

agupubs.onlinelibrary.wiley.com/doi/abs/10.1029/2020AV000275 (e2020AV000275 2020AV000275) doi: https://doi.org/10.1029/2020AV000275

Chané, E., Palmaerts, B., & Radioti, A. (2018, September). Periodic shearing motions in the Jovian magnetosphere causing a localized peak in the main auroral emission close to noon. *Planetary and Space Science*, *158*, 110-117. doi: 10.1016/j.pss.2018.04.023

Chané, E., Saur, J., Keppens, R., & Poedts, S. (2017, February). How is the Jovian main auroral emission affected by the solar wind? *Journal of Geophysical Research (Space Physics)*, *122*(2), 1960-1978. doi: 10.1002/2016JA023318

Clarke, J. T., Ballester, G., Trauger, J., Ajello, J., Pryor, W., Tobiska, K., ... Gérard, J.-C. (1998). Hubble space telescope imaging of jupiter's uv aurora during the galileo orbiter mission. *Journal of Geophysical Research: Planets*, *103*(E9), 20217-20236. Retrieved from https://agupubs.onlinelibrary.wiley.com/doi/abs/10.1029/98JE01130 doi: 10.1029/98JE01130

Clarke, J. T., Grodent, D., Cowley, S. W. H., Bunce, E. J., Zarka, P., Connerney, J. E. P., & Satoh, T. (2004). Jupiter's aurora. In F. Bagenal, T. E. Dowling, & W. B. McKinnon (Eds.), *Jupiter. the planet, satellites and magnetosphere* (Vol. 1, p. 639-670).

Clarke, J. T., Nichols, J., Gérard, J. C., Grodent, D., Hansen, K. C., Kurth, W., ... Cecconi, B. (2009, May). Response of Jupiter's and Saturn's auroral activity to the solar wind. *Journal of Geophysical Research (Space Physics)*, *114*(A5), A05210. doi: 10.1029/2008JA013694

Connerney, J. E. P., Kotsiaros, S., Oliversen, R. J., Espley, J. R., Joergensen, J. L., Joergensen, P. S., ... Levin, S. M. (2018, March). A New Model of Jupiter's Magnetic Field From Juno's First Nine Orbits. *Geophysical Research Letters*, *45*(6), 2590-2596. doi: 10.1002/2018GL077312

Cowley, S., & Bunce, E. (2001). Origin of the main auroral oval in jupiter's coupled magnetosphere–ionosphere system. *Planetary and Space Science*, *49*(10), 1067 - 1088. Retrieved from http://www.sciencedirect.com/science/article/pii/S0032063300001677 (Magnetosphere of the Outer Planets Part II) doi: https://doi.org/10.1016/S0032-0633(00)00167-7

Gérard, J.-C., Dols, V., Prangé, R., & Paresce, F. (1994, November). The morphology of the north Jovian ultraviolet aurora observed with the Hubble Space Telescope. *Planetary and Space Science*, *42*(11), 905-917. doi: 10.1016/0032-0633(94)90051-5

Gérard, J. C., Gkouvelis, L., Bonfond, B., Grodent, D., Gladstone, G. R., Hue, V., ... Blanc, M. (2020, August). Spatial Distribution of the Pedersen Conductance in the Jovian Aurora From Juno-UVS Spectral Images. *Journal of Geophysical Research (Space Physics)*, *125*(8), e28142. doi: 10.1029/2020JA028142

Grodent, D. (2015, April). A Brief Review of Ultraviolet Auroral Emissions on Giant Planets. *Space Science Reviews*, *187*(1-4), 23-50. doi: 10.1007/s11214-014-0052-8

Grodent, D., Bonfond, B., Gérard, J.-C., Radioti, A., Gustin, J., Clarke, J. T., ... Connerney, J. E. P. (2008, September). Auroral evidence of a localized magnetic anomaly in Jupiter's northern hemisphere. *Journal of Geophysical Research (Space Physics)*, *113*(A9), A09201. doi: 10.1029/2008JA013185

Grodent, D., Bonfond, B., Yao, Z., Gérard, J. C., Radioti, A., Dumont, M., ... Valek, P. (2018, May). Jupiter's Aurora Observed With HST During Juno Orbits 3 to 7. *Journal of Geophysical Research (Space Physics)*, *123*(5), 3299-3319. doi: 10.1002/2017JA025046

Grodent, D., Clarke, J. T., Kim, J., Waite Jr., J. H., & Cowley, S. W. H. (2003). Jupiter's main auroral oval observed with hst-stis. *Journal of Geophysical Research: Space Physics*, *108*(A11). Retrieved from https://agupubs.onlinelibrary.wiley.com/doi/abs/10.1029/2003JA009921 doi:

10.1029/2003JA009921
Grodent, D., Gérard, J. C., Cowley, S. W. H., Bunce, E. J., & Clarke, J. T. (2005, July). Variable morphology of Saturn's southern ultraviolet aurora. *Journal of Geophysical Research (Space Physics)*, *110*(A7), A07215. doi: 10.1029/2004JA010983
Grodent, D., Gladstone, G. R., Gérard, J. C., Dols, V., & Waite, J. H. (1997, August). Simulation of the Morphology of the Jovian UV North Aurora Observed with the Hubble Space Telescope. *Icarus*, *128*(2), 306-321. doi: 10.1006/icar.1997.5740
Grodent, D., Gérard, J.-C., Radioti, A., Bonfond, B., & Saglam, A. (2008). Jupiter's changing auroral location. *Journal of Geophysical Research: Space Physics*, *113*(A1). Retrieved from `https://agupubs.onlinelibrary.wiley.com/doi/abs/10.1029/2007JA012601` doi: https://doi.org/10.1029/2007JA012601
Gustin, J., Bonfond, B., Grodent, D., & Gérard, J. C. (2012, September). Conversion from HST ACS and STIS auroral counts into brightness, precipitated power and radiated power for H2 giant planets. In *European planetary science congress 2012* (p. EPSC2012-54).
Gustin, J., Cowley, S. W. H., Gérard, J. C., Gladstone, G. R., Grodent, D., & Clarke, J. T. (2006, September). Characteristics of Jovian morning bright FUV aurora from Hubble Space Telescope/Space Telescope Imaging Spectrograph imaging and spectral observations. *Journal of Geophysical Research (Space Physics)*, *111*(A9), A09220. doi: 10.1029/2006JA011730
Hill, T. W. (2001, May). The Jovian auroral oval. *Journal of Geophysical Research (Space Physics)*, *106*(A5), 8101-8108. doi: 10.1029/2000JA000302
Joy, S. P., Kivelson, M. G., Walker, R. J., Khurana, K. K., Russell, C. T., & Ogino, T. (2002, October). Probabilistic models of the Jovian magnetopause and bow shock locations. *Journal of Geophysical Research (Space Physics)*, *107*(A10), 1309. doi: 10.1029/2001JA009146
Kimura, T., Hiraki, Y., Tao, C., Tsuchiya, F., Delamere, P. A., Yoshioka, K., . . . Fujimoto, M. (2018, March). Response of Jupiter's Aurora to Plasma Mass Loading Rate Monitored by the Hisaki Satellite During Volcanic Eruptions at Io. *Journal of Geophysical Research (Space Physics)*, *123*(3), 1885-1899. doi: 10.1002/2017JA025029
Kimura, T., Nichols, J. D., Gray, R. L., Tao, C., Murakami, G., Yamazaki, A., . . . Fujimoto, M. (2017, May). Transient brightening of Jupiter's aurora observed by the Hisaki satellite and Hubble Space Telescope during approach phase of the Juno spacecraft. *Geophysical Research Letters*, *44*(10), 4523-4531. doi: 10.1002/2017GL072912
Kita, H., Kimura, T., Tao, C., Tsuchiya, F., Misawa, H., Sakanoi, T., . . . Fujimoto, M. (2016, July). Characteristics of solar wind control on Jovian UV auroral activity deciphered by long-term Hisaki EXCEED observations: Evidence of preconditioning of the magnetosphere? *Geophysical Research Letters*, *43*(13), 6790-6798. doi: 10.1002/2016GL069481
Knight, S. (1973, May). Parallel electric fields. *Planetary and Space Science*, *21*(5), 741-750. doi: 10.1016/0032-0633(73)90093-7
Krupp, N., Lagg, A., Livi, S., Wilken, B., Woch, J., Roelof, E. C., & Williams, D. J. (2001, November). Global flows of energetic ions in Jupiter's equatorial plane: First-order approximation. *Journal of Geophysical Research (Space Physics)*, *106*(A11), 26017-26032. doi: 10.1029/2000JA900138
Lorch, C. T. S., Ray, L. C., Arridge, C. S., Khurana, K. K., Martin, C. J., & Bader, A. (2020, February). Local Time Asymmetries in Jupiter's Magnetodisc Currents. *Journal of Geophysical Research (Space Physics)*, *125*(2), e27455. doi: 10.1029/2019JA027455
Mauk, B. H., Clark, G., Gladstone, G. R., Kotsiaros, S., Adriani, A., Allegrini, F., . . . Rymer, A. M. (2020, March). Energetic Particles and Acceleration

Regions Over Jupiter's Polar Cap and Main Aurora: A Broad Overview. *Journal of Geophysical Research (Space Physics)*, *125*(3), e27699. doi: 10.1029/2019JA027699

Mauk, B. H., Haggerty, D. K., Paranicas, C., Clark, G., Kollmann, P., Rymer, A. M., ... Valek, P. (2017, September). Discrete and broadband electron acceleration in Jupiter's powerful aurora. *Nature*, *549*(7670), 66-69. doi: 10.1038/nature23648

Mauk, B. H., Haggerty, D. K., Paranicas, C., Clark, G., Kollmann, P., Rymer, A. M., ... Valek, P. (2018, February). Diverse Electron and Ion Acceleration Characteristics Observed Over Jupiter's Main Aurora. *Geophysical Research Letters*, *45*(3), 1277-1285. doi: 10.1002/2017GL076901

Millward, G., Miller, S., Stallard, T., Aylward, A. D., & Achilleos, N. (2002, November). On the Dynamics of the Jovian Ionosphere and Thermosphere. III. The Modelling of Auroral Conductivity. *Icarus*, *160*(1), 95-107. doi: 10.1006/icar.2002.6951

Nichols, J. D., Allegrini, F., Bagenal, F., Bunce, E. J., Cowley, S. W. H., Ebert, R. W., ... Yao, Z. (2020, August). An Enhancement of Jupiter's Main Auroral Emission and Magnetospheric Currents. *Journal of Geophysical Research (Space Physics)*, *125*(8), e27904. doi: 10.1029/2020JA027904

Nichols, J. D., Clarke, J. T., Gérard, J. C., Grodent, D., & Hansen, K. C. (2009, June). Variation of different components of Jupiter's auroral emission. *Journal of Geophysical Research (Space Physics)*, *114*(A6), A06210. doi: 10.1029/2009JA014051

Nichols, J. D., & Cowley, S. W. H. (2022). Relation of jupiter's dawnside main emission intensity to magnetospheric currents during the juno mission. *Journal of Geophysical Research: Space Physics*, *127*(1), e2021JA030040. Retrieved from `https://agupubs.onlinelibrary.wiley.com/doi/abs/10.1029/2021JA030040` (e2021JA030040 2021JA030040) doi: https://doi.org/10.1029/2021JA030040

Nichols, J. D., Yeoman, T. K., Bunce, E. J., Chowdhury, M. N., Cowley, S. W. H., & Robinson, T. R. (2017, September). Periodic Emission Within Jupiter's Main Auroral Oval. *Geophysical Research Letters*, *44*(18), 9192-9198. doi: 10.1002/2017GL074824

Palmaerts, B., Radioti, A., Grodent, D., Chané, E., & Bonfond, B. (2014, December). Transient small-scale structure in the main auroral emission at Jupiter. *Journal of Geophysical Research (Space Physics)*, *119*(12), 9931-9938. doi: 10.1002/2014JA020688

Prangé, R., Zarka, P., Ballester, G. E., Livengood, T. A., Denis, L., Carr, T., ... Moos, H. W. (1993, October). Correlated variations of UV and radio emissions during an outstanding Jovian auroral event. *Journal of Geophysical Research (Space Physics)*, *98*(E10), 18779-18792. doi: 10.1029/93JE01802

Radioti, A., Gérard, J. C., Grodent, D., Bonfond, B., Krupp, N., & Woch, J. (2008, January). Discontinuity in Jupiter's main auroral oval. *Journal of Geophysical Research (Space Physics)*, *113*(A1), A01215. doi: 10.1029/2007JA012610

Ray, L. C., Achilleos, N. A., Vogt, M. F., & Yates, J. N. (2014). Local time variations in jupiter's magnetosphere-ionosphere coupling system. *Journal of Geophysical Research: Space Physics*, *119*(6), 4740-4751. Retrieved from `https://agupubs.onlinelibrary.wiley.com/doi/abs/10.1002/2014JA019941` doi: 10.1002/2014JA019941

Southwood, D. J., & Kivelson, M. G. (2001, April). A new perspective concerning the influence of the solar wind on the Jovian magnetosphere. *Journal of Geophysical Research (Space Physics)*, *106*(A4), 6123-6130. doi: 10.1029/2000JA000236

Swithenbank-Harris, B. G., Nichols, J. D., Allegrini, F., Bagenal, F., Bonfond, B., Bunce, E. J., ... Wilson, R. J. (2021). Simultaneous observation of an auroral dawn storm with the hubble space telescope and juno. *Journal of Geophysical Research: Space Physics*, *126*(4), e2020JA028717. Retrieved from `https://agupubs.onlinelibrary.wiley.com/doi/abs/10.1029/2020JA028717` (e2020JA028717 2020JA028717) doi: https://doi.org/10.1029/2020JA028717

Tao, C., Fujiwara, H., & Kasaba, Y. (2010, February). Jovian magnetosphere-ionosphere current system characterized by diurnal variation of ionospheric conductance. *Planetary and Space Science*, *58*(3), 351-364. doi: 10.1016/j.pss.2009.10.005

Thomas, N., Bagenal, F., Hill, T. W., & Wilson, J. K. (2004). The Io neutral clouds and plasma torus. In F. Bagenal, T. E. Dowling, & W. B. McKinnon (Eds.), *Jupiter. the planet, satellites and magnetosphere* (Vol. 1, p. 561-591).

Vincent, M. B., Clarke, J. T., Ballester, G. E., Harris, W. M., West, R. A., Trauger, J. T., . . . Westphal, J. A. (2000). Mapping jupiter's latitudinal bands and great red spot using hst/wfpc2 far-ultraviolet imaging. *Icarus*, *143*(2), 189-204. Retrieved from `https://www.sciencedirect.com/science/article/pii/S0019103599962322` doi: https://doi.org/10.1006/icar.1999.6232

Waite, J. H., Gladstone, G. R., Lewis, W. S., Goldstein, R., McComas, D. J., Riley, P., . . . Young, D. T. (2001, April). An auroral flare at Jupiter. *Nature*, *410*(6830), 787-789.

Yao, Z. H., Bonfond, B., Clark, G., Grodent, D., Dunn, W. R., Vogt, M. F., . . . Bolton, S. J. (2020, August). Reconnection- and Dipolarization-Driven Auroral Dawn Storms and Injections. *Journal of Geophysical Research (Space Physics)*, *125*(8), e27663. doi: 10.1029/2019JA027663

Figure 1.

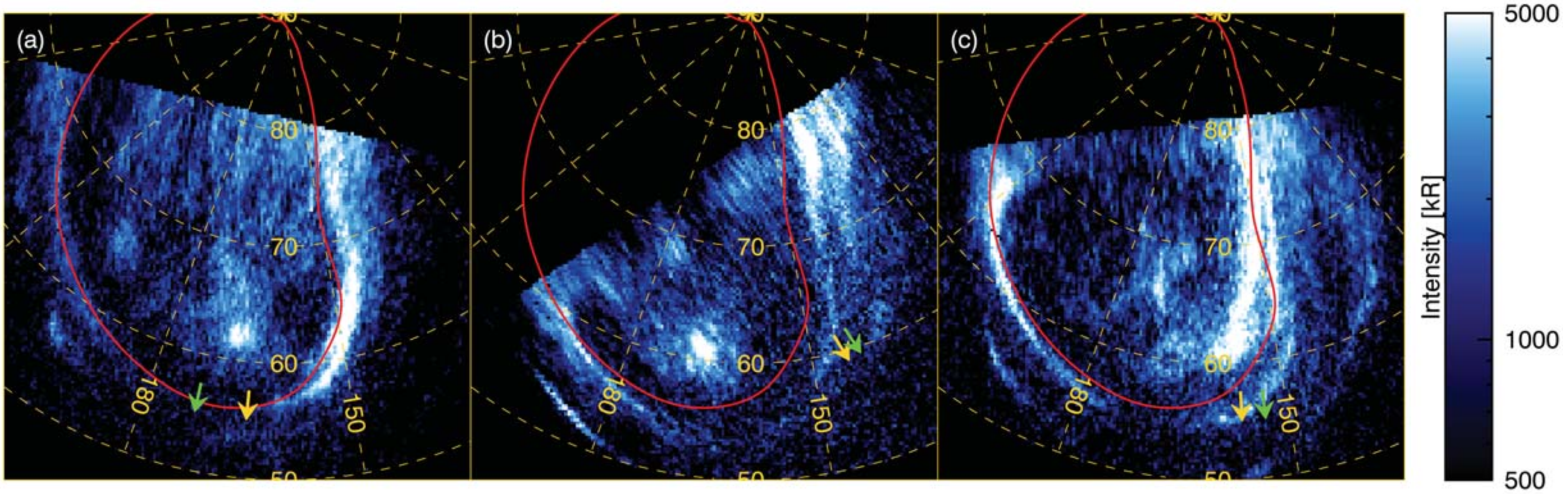

(a)
(b)
(c)
80
70
60
50
180
150
Intensity [kR]
5000
1000
500

Figure 2.

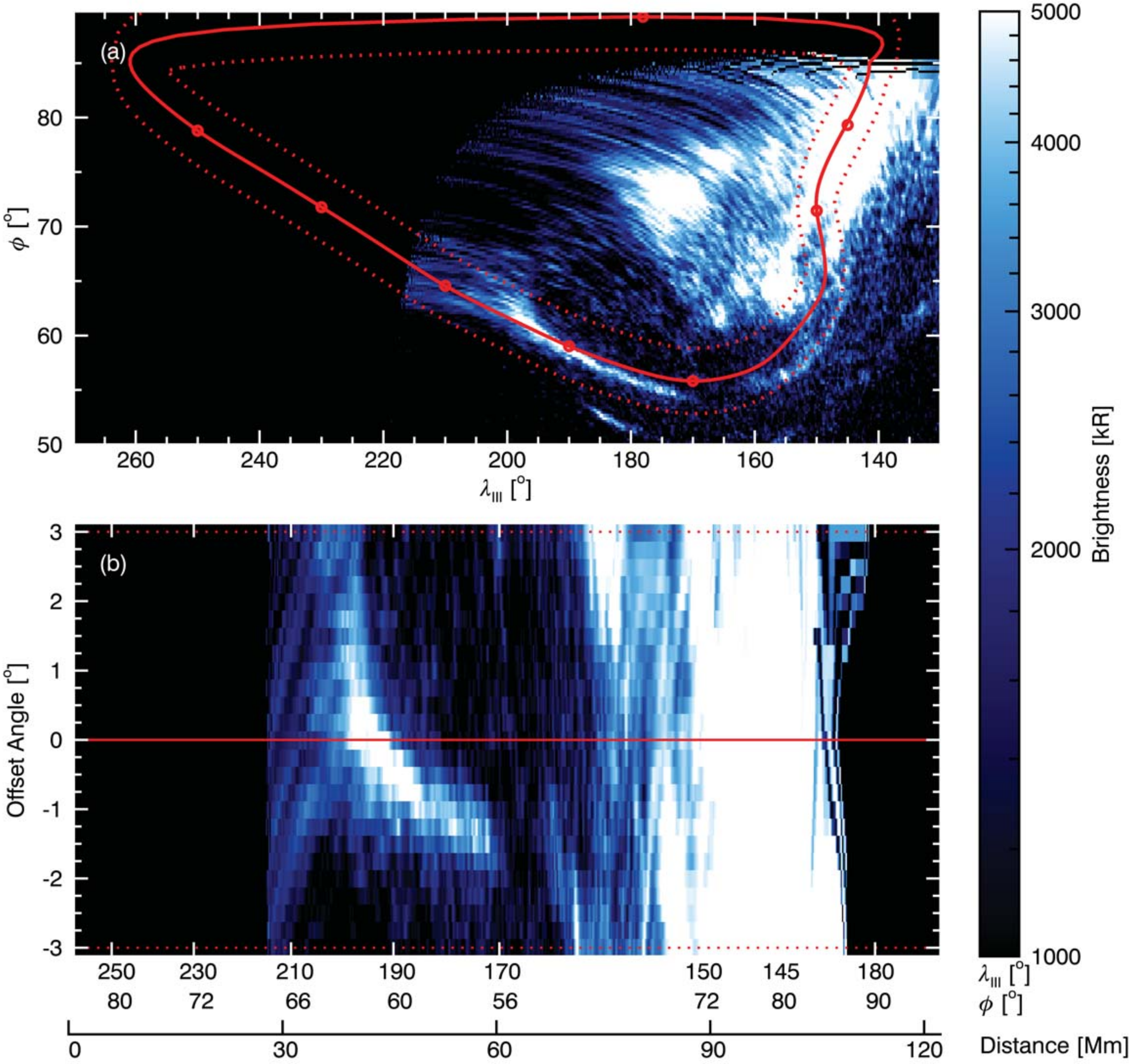
(a)
φ [°]
λ_III [°]
(b)
Offset Angle [°]
250 230 210 190 170 150 145 180
80 72 66 60 56 72 80 90
0 30 60 90 120
λ_III [°]
φ [°]
Distance [Mm]
Brightness [kR]
1000 2000 3000 4000 5000

Figure 3.

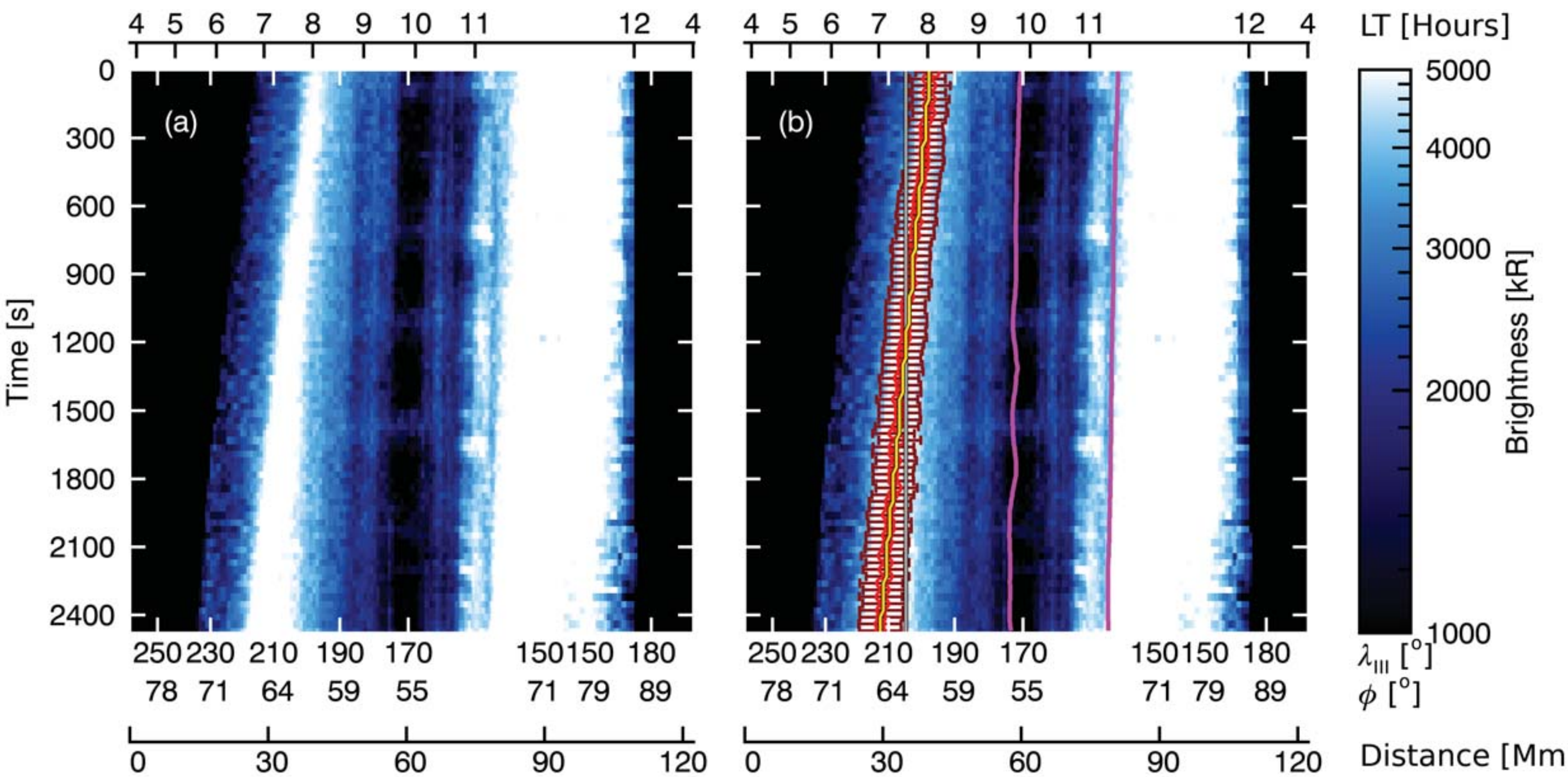

LT [Hours]
4 5 6 7 8 9 10 11 12 4
(a)
(b)
Time [s]
0 300 600 900 1200 1500 1800 2100 2400
250 230 210 190 170 150 150 180
78 71 64 59 55 71 79 89
λ_{III} [°]
ϕ [°]
0 30 60 90 120
Distance [Mm]
Brightness [kR]
5000 4000 3000 2000 1000

Figure 4.

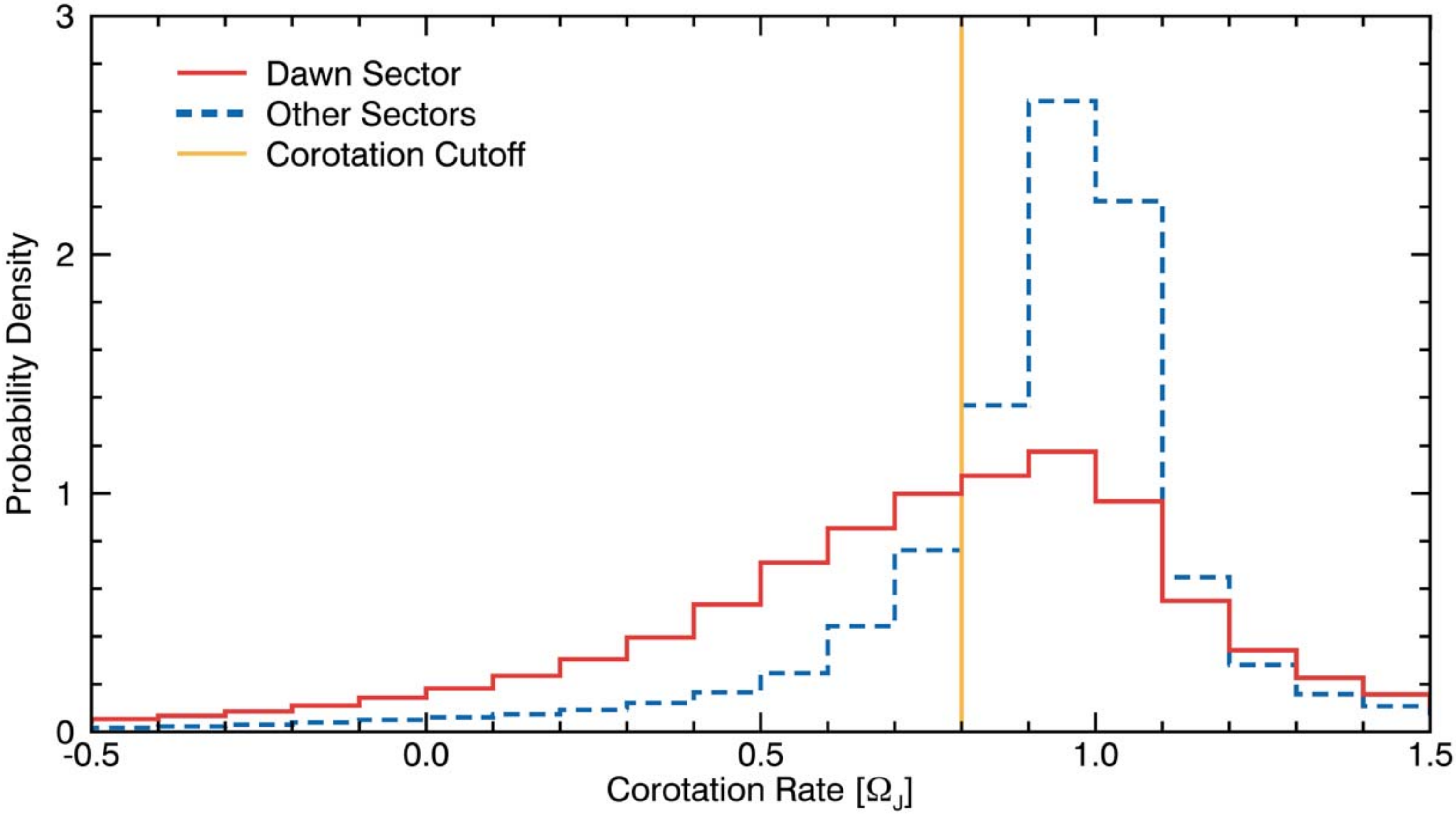
Dawn Sector
Other Sectors
Corotation Cutoff
Probability Density
Corotation Rate [Ω_J]
3
2
1
0
-0.5
0.0
0.5
1.0
1.5

Figure 5.

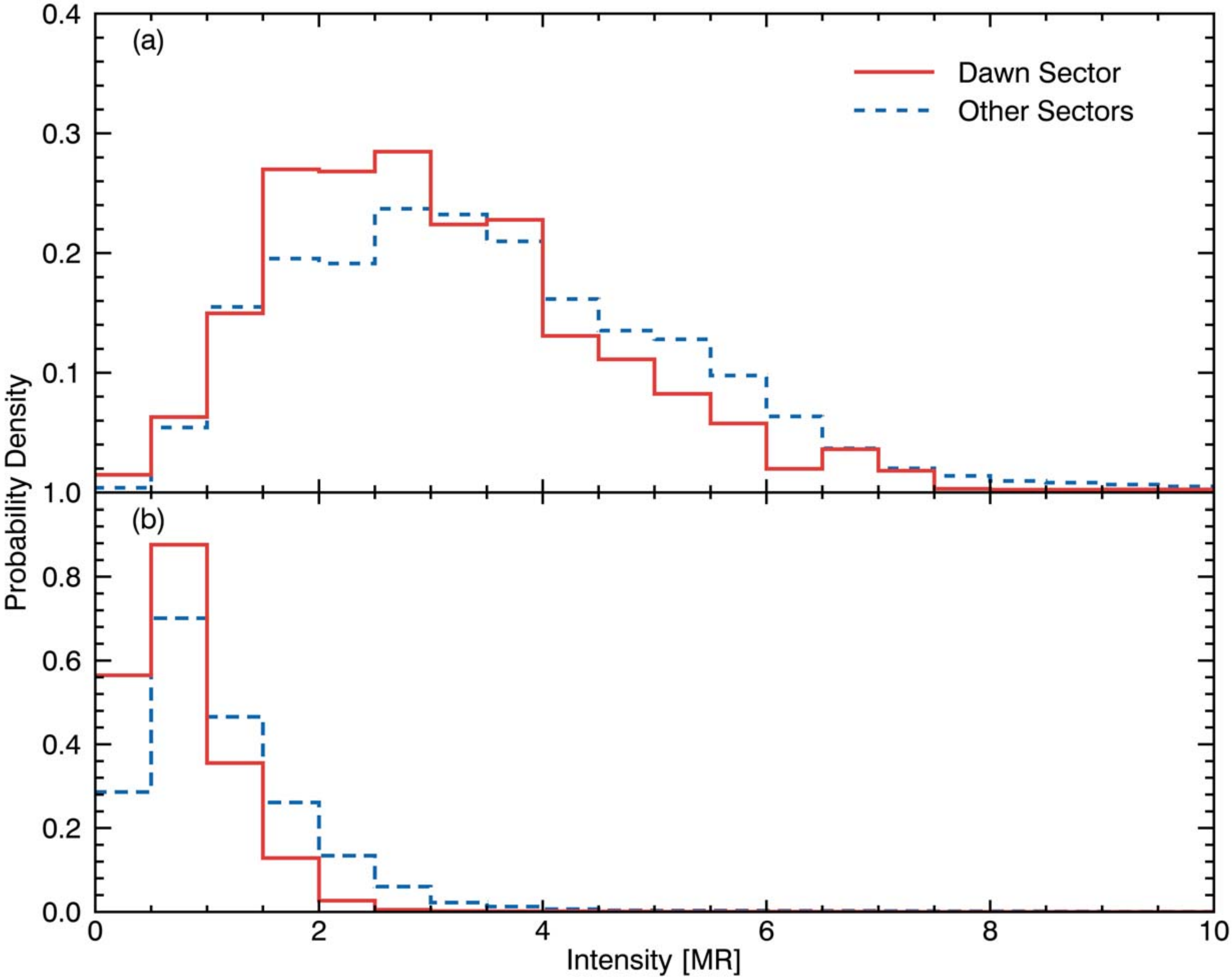

(a)
(b)
Dawn Sector
Other Sectors
Probability Density
Intensity [MR]
0.4
0.3
0.2
0.1
1.0
0.8
0.6
0.4
0.2
0.0
0
2
4
6
8
10